



A Test Fixture to Measure the Skin Friction of Anisotropic Surfaces

Brad Rafferty¹, and Bob Dowgwillo².
The Boeing Company, Berkeley, Missouri, 63134, United States

Boeing Research & Technology (BR&T) St. Louis has completed a series of tests on a unique wind tunnel fixture designed by BR&T and Boeing Test & Evaluation (BT&E) St. Louis to reliably and repeatably measure the average skin friction coefficient, C_F , of any given surface specimen as a function of flow angle. The tests, conducted in the Advanced Aeromechanical Control Effector Systems (AACES) Lab, are executed on five unique surface specimens: smooth metal (as a baseline), smooth film, uniform roughness (sandpaper), and two different anisotropic films. The C_F of the baseline and the smooth film are nearly identical and agree well with theory. The C_F of the baseline, smooth film, and uniform roughness are all statistically independent of flow angle. The C_F of the anisotropic films depends on angle with statistical significance, with the maximum C_F of the films more than twice that of the baseline. The novel test fixture is shown to agree well with smooth, flat-plate, turbulent boundary-layer theory and to be repeatable. This capability offers a valuable capability for skin friction characterization of a wide range of surface specimens and features at any flow yaw angle.

Nomenclature

A	=	pressure gradient parameter
B	=	turbulent wall-law intercept constant
C_f	=	local skin friction coefficient
C_F	=	average skin friction coefficient
C_v	=	coefficient of variance
H	=	shape factor
f	=	Coles wake function
k	=	average roughness height, inches
M	=	Mach number
p	=	pressure, psi
P	=	precision limit
p_v	=	P-value
R^2	=	R-squared
Re	=	Reynolds number
T	=	temperature, F
u	=	velocity; $u = u(x, y)$, ft/s
u_τ	=	wall friction velocity, ft/s
x	=	coordinate of longitudinal or streamwise direction of flow; along the length of the splitter plate, inches
y	=	coordinate normal to wall; height, inches
z	=	coordinate of lateral direction; along the span of the splitter plate, inches
ψ	=	yaw angle of material with respect to freestream flow, degrees
β	=	Clauser similarity parameter
δ	=	boundary layer thickness, inches
δ^*	=	displacement thickness, inches
κ	=	Kármán constant

¹ Aerodynamics Engineer, Boeing Research & Technology, AIAA Member, bradley.rafferty@boeing.com

² Technical Lead Aerodynamics Engineer, Boeing Research & Technology, AIAA Associate Fellow

Π	=	Coles wake parameter
σ	=	standard deviation
τ_w	=	shear stress at wall, lbf/ft ²
θ	=	momentum thickness, inches
ν	=	kinematic viscosity, ft ² /s

Subscripts

1	=	location at upstream rake
2	=	location at downstream rake
e	=	location at boundary layer edge
t	=	total
∞	=	freestream

Superscripts

$-$	=	time-averaged
$+$	=	law-of-the-wall variable

I. Introduction

For over a century, theorists and experimentalists have deduced and devised methods to estimate and measure aerodynamic drag. Of particular interest is the estimation of skin friction drag, wherein countless efforts undertake the exacting challenge of estimating the skin friction coefficient at a point or over a body.

A variety of methods exist to overcome this challenge, most notably: oil film interferometry (OFI), hot wire anemometry, Preston tubes, and floating element balances. The authors direct the reader to overviews such as those by Fernholz or Naughton [1, 2] for a more complete discussion of such methods, but would like to briefly mention some shortcomings of the aforementioned techniques. OFI spreads a thin oil film over the subject surface and aims to detect the thinning rate of the film and, hence, deduce the forces acting on the film caused by the airflow [3]. It requires a camera to be accurately spatially-calibrated, requires accurate knowledge of the oil properties (including how they may change during a test), may suffer from potential oil contamination by fine particles, necessitates relatively heavy image post-processing, and the oil cannot be applied to a non-smooth specimen. Hot wire anemometry can be used to determine mean velocity profiles via a traverse method. These profiles are then used to calculate skin friction parameters of interest. Hot wires, however, require tedious calibration and are inherently fragile instrumentation. Additionally, survey-based methods—with hot wires or other instrumentation—are susceptible to calibration errors if test conditions drift as the survey is progressing. Preston tubes are a fine choice for comparing to results from other, principal instrumentation, but they rely on the accuracy of the calibration and each tube only measures at a single location. Lastly, floating element balances require highly-accurate force measurement and typically are limited in accuracy by the precision of their mechanical installation. Additionally, there are some types that do not adjust well to temperature or nonzero-pressure-gradients. The authors believe that, in comparison to aforementioned methods, a momentum-based method offers a practical balance between accuracy and ease of installation and operation for estimating C_F over any arbitrary surface condition for a wide range of operating regimes [4-6]. Drawbacks of a boundary-layer rake method are that it requires accurate measurements of pressure and of each probe height, and that rakes are typically not suitable for measuring in the viscous sublayer.

The ability to estimate C_F for arbitrary surface conditions offers valuable knowledge about the effects of various surface qualities—be it a new paint, parasitic materials such as riblet film, or even simulating seams and gaps in a material—on the drag and, hence, performance of an air vehicle. Surprisingly, consideration of the dependence of C_F on flow angle is largely unaddressed in the literature despite the potentially-significant coupling between the drag contribution of the surface specimen and the angle at which it presents itself with respect to the local surface flow. Additionally, skin friction test fixtures often lack modularity inasmuch as each fixture is typically unique to the test article, or the fixture itself is a representative model of a product, thus requiring a disproportionate investment in the configuration of the test relative to the testing itself. To the authors' knowledge, there is not presented in the literature a fixture that has the capability to readily measure the average skin friction coefficient of an arbitrary surface specimen at any flow angle, on-command.

II. Experiment Setup

A. AACES Lab Wind Tunnel

The AACES Lab Wind Tunnel (ALWT), pictured in Fig. 1, is a research-quality, closed-loop, low-speed wind tunnel with key specifications listed in Table 1. The ALWT ceiling panels are adjustable in height and angle, which is a particularly important means to adjust the boundary layer pressure gradient over the test fixture splitter plate. A total-temperature Pitot-static probe is stationed at the x -location of the leading edge of the splitter plate and at the y -location midway between the top of the splitter plate and the ceiling of the tunnel. The u calculated from this Pitot-static probe is used to control the tunnel to a target u_∞ or unit Re . For the testing of interest here, controlling to a unit Re allows for a more repeatable test compared to controlling to u_∞ . For this reason, a new control software is developed to control the tunnel to a unit Re setpoint by adjusting the tunnel fan speed, and thereby u_∞ , to compensate for any slight drifts in test section temperature over the course of a long test run.



Fig. 1 AACES Lab Wind Tunnel

The tunnel accommodates a plywood false-wall that allows the pass-through of electronics cables and pressure tubing from the test fixture to outside of the tunnel without disturbing the flow.

Table 1 Key specifications of the ALWT

Test Section Dimensions	27.5" (floor to ceiling) x 36" (wall to wall) x 144"
Max q_∞	26 psf
Max u_∞	155 ft/s
Max M_∞	0.14
Max Unit Re	8.95×10^5 /ft
Turbulence Intensity	< 1.5%
Flow Angularity at 150 ft/s	$\theta = -0.19^\circ$ (+/- .03°) pitch down $\psi = -0.03^\circ$ (+/- .02°) yaw counter clockwise

B. Test Fixture

This section overviews the various key features of the test fixture: the splitter plate with a removable, inset rotatable disk, the boundary layer trip strip, the measurement equipment, and the tested specimens.

1. Splitter Plate

The fixture, shown in Fig. 2, is a smooth aluminum splitter plate raised on struts to avoid the boundary layer of the tunnel floor. The splitter plate is 36" wide and 53" long with an inset 24"-diameter rotatable disk whose upstream edge is 24" downstream of the splitter plate leading edge. The leading edge is a super ellipse design intended to accommodate some flow angularity while also avoiding large local pressure gradients caused by rapid changes in surface radius of curvature. The splitter plate pitch angle with respect to the tunnel floor can be adjusted by shimming the front or back struts as desired to help achieve a zero-pressure-gradient. This feature affords a complementary degree of flow adjustment in addition to wind tunnel ceiling panel settings. The quarter-inch gap between the splitter plate sides and wind tunnel walls is sealed using an adhesive-backed foam. This proves to be an important detail in tuning the longitudinal pressure gradient over the plate. The feasibility and design decisions for splitter plate smooth-run length, the rotatable-disk diameter, the boundary-layer rake probe heights, and the data reduction process are supported by an iterative MATLAB simulation. The simulation exercises flat-plate, laminar and turbulent boundary-layer theory at the conditions of the ALWT—unit Re , M_∞ , and u_∞ . Detailed design of the fixture is a balance of functionality, minimal blockage, flow quality, and cost.

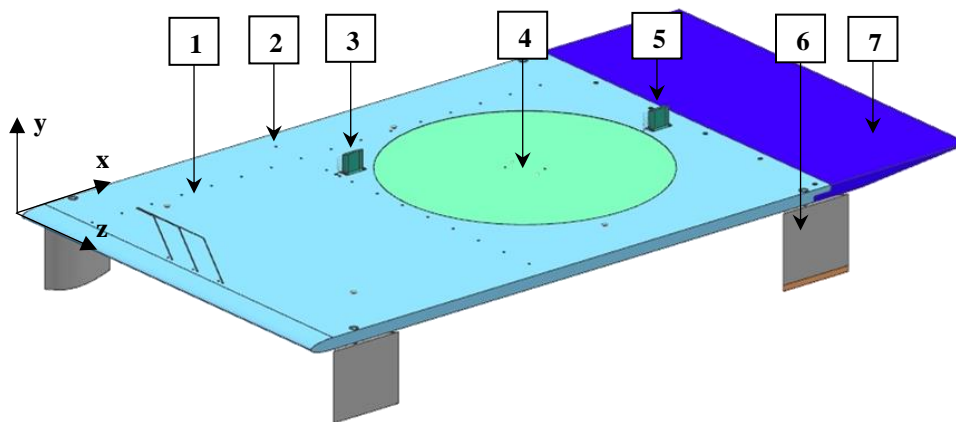


Fig. 2 Test fixture CAD model. (1) Splitter plate; (2) static pressure tap; (3) upstream rake; (4) rotatable disk; (5) downstream rake; (6) strut; (7) removable trailing edge

2. Boundary Layer Trip Strip

The trip strip is a one-dimensional array of short cylinders approximately 1.5" downstream of the splitter plate leading edge and designed per Ref. [7]. This trip strip robustly and uniformly trips the flow at the desired unit Re to promote a uniform, turbulent boundary layer over the surface specimen. The trip strip functionality is validated via infrared thermography. Figure 3 illustrates this validation process and similar applications of IR thermography can be

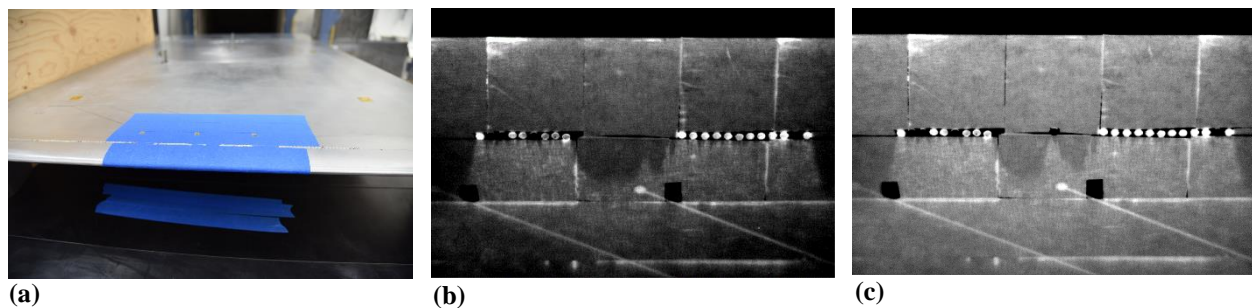


Fig. 3 Boundary-layer trip-strip validation process. (a) View of leading edge, looking downstream (b) IR image at test conditions, air flows top to bottom; (c) an additional dot is added to the middle of the frame

found in the literature [8, 9]. Tape covers the aluminum splitter plate surface to increase the emissivity for proper functionality of the IR camera. The turbulent transition is detected behind the trip strip via the IR thermography because the turbulent mixing increases the heat transfer coefficient and thus the thermal gradient in front of after the trip. The addition of another, singular dot in the middle of the area of interest and its production of a clear, cone-shaped wake added further confirms the success of the trip strip. The two-dimensionality of the flow is assessed via the spanwise equivalent u_e , which is discussed in Section III.A.1.

3. Pressure Measurements

The principal test fixture instrumentation consists of two fixed boundary-layer rakes, located just upstream and just downstream of the rotating disk. Each rake, as seen in Fig. 4, is equipped with 18 total pressure probes, the lowest of which is designed to be 0.023" above the splitter plate and the highest of which 1.465" above the splitter plate; each rake fully captures the entire y -extent of the turbulent boundary layers produced in this testing.

To account for slight misalignments in rake probe y -locations, the test operator measures the as-built heights of each of the 36 rake probes to an accuracy of ± 0.001 " and uses the measured values for calculations of boundary-layer parameters that depend on height. Rake total pressures are measured with an accuracy of ± 0.005 psi.

In addition, the splitter plate is fitted with 34 static-pressure taps to diagnose flow quality: 16 longitudinal (streamwise) taps, 13 lateral taps (one of which doubles as a longitudinal tap), and three taps on the top and bottom surface each just downstream of the leading edge. Each static-pressure tap was inspected for defects with a digital microscope and both the static taps and total pressure probes are cleared of debris using compressed air. All pressure lines are leak checked. Splitter plate static pressures are measured to an accuracy of ± 0.005 psi. Tunnel conditions are measured to an accuracy of ± 0.00036 psi. In future testing, all pressures will be measured to an accuracy of ± 0.00036 psi or better.

Diagnostic data for this experiment readily identifies one pinched pressure tubing line and one disconnected pressure tubing line within the test fixture—rake 1 probes 6 and 7, respectively. These data are omitted from analyses following a decision to avoid test disruption caused by the need to disassemble the fixture from the tunnel to replace the aforementioned lines. Future testing will include more rigorous pressure tubing check-out before test fixture installation.

4. Material Specimens

In normal operation, a material specimen is adhered to a steel disk that is then inset into the splitter plate. The disk is shimmed such that only the roughness pattern of the specimen protrudes above the splitter plate top surface, i.e. a smooth specimen would ideally be completely flush with the splitter plate surface. However, even a particular commercial precision-ground disk may not be flat enough. If a small protrusion occurs, the disk is shimmed to accommodate the smallest protrusion or, ideally, only backward-facing steps. The disk rides on Teflon pads and shims are arranged under the pads to obtain the most level disk top surface possible, as measured by a height gage before each test.

A remotely-operated electric motor rotates the disk to any desired ψ . The motor is housed within a specially-designed fairing on the lower surface of the test fixture. It permits faster assembly and avoids the complications of utilizing the existing floor-mounted turntable.

Tests are executed on five different surface specimens: smooth metal (as a baseline), smooth film, uniform roughness (sandpaper), and two anisotropic films. The sandpaper grit size is chosen to match the approximate feature height of the anisotropic films to facilitate comparison of results. Figure 5 is of the sandpaper specimen installed in the test fixture.

The two anisotropic films feature repeating patterns of homogeneous extrusions across their extent, with the span of the patterns perpendicular to incoming air flow at $\psi = 0$ and $\psi = 180$ and the span of the patterns parallel to the incoming air flow at $\psi = 90$ and $\psi = 270$. Due to the nature of manufacture of the anisotropic films, they are applied as two halves or four quarters of the disk surface area. Similarly, the sandpaper is applied in 8"x10" sheets until the whole metal disk surface is covered. This application method is not ideal as it creates seams in these material specimens—some more significant than others—whereas the smooth film is applied as a single piece across the extent of the disk surface. The effect of seams is discussed in Section III.B.

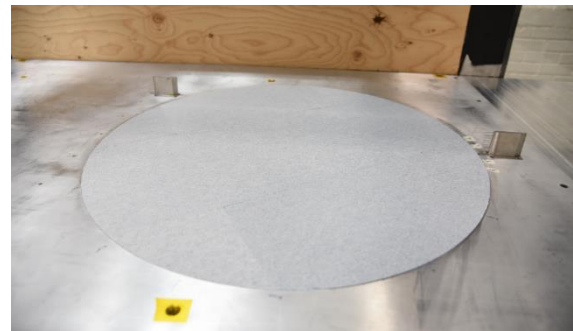


Fig. 5 Sandpaper specimen installed into fixture

C. Test Conditions

The test plan is defined in conformity with Design of Experiments practice. Test runs consist of sweeping through 180° in two blocks with ψ set randomly within each block. The blocks are intended to reduce waiting time for the

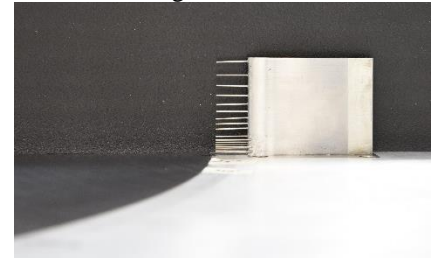


Fig. 4 Close-up of downstream rake

electric motor to move to a setpoint and to potentially identify data dependencies on time. Sixty samples are recorded at each ψ at a one-Hz sampling rate. Replicates are collected to assess pure error. The fixture and test are designed to avoid block effects arising from prolonging a single test run over different days. The 180° sweeps (36 unique ψ) require only two hours of testing, including at least five replicate runs. Sweeps of 360° at 5° increments are estimated to require approximately four hours of testing.

All five disks are tested at approximately the same unit Re of $8.90 \times 10^5/\text{ft}$ which corresponds to a M_∞ of approximately 0.14. Throughout a run, either the u_∞ or the unit Re is held constant. The metal and smooth-film specimens are tested with constant- u_∞ control while the sandpaper and anisotropic films are tested with the unit- Re controller and set to a unit Re that matches preceding tests. At the time of testing the metal and smooth-film specimens, the unit Re controller was not yet established. By the nature of the test process and tunnel conditions, the unit Re is nearly identical across all test runs despite the different control methods. This comparability is addressed in III.A.1. With reassurance of the near-identical test conditions, tests are not repeated on the first two specimens. Results in the metal and smooth film disks that trend (slightly) with time over long tests are readily correlated with the same (slight) trend in test section Re . Future testing will utilize only unit Re control and will control to past unit Re measurements.

D. Calculations and Assumptions

The intent of this section is to outline the method by which C_F and diagnostic parameters are calculated as well as key assumptions that are made in those calculations.

1. Calculations

For each test condition, the rake u profiles are calculated from the total pressure measured by each rake probe, the average of local static surface pressures, and density determined from conditions at the test section Pitot-static-temperature probe. Using these u profiles, δ , δ^* , θ , and H are calculated at the upstream and downstream rakes, where

$$\delta = y(\bar{u} = 0.99 * \bar{u}_e) \quad (1)$$

$$\delta^* = \int_0^\infty \left(1 - \frac{\bar{u}}{\bar{u}_e}\right) dy \quad (2)$$

$$\theta = \int_0^\infty \frac{\bar{u}}{\bar{u}_e} \left(1 - \frac{\bar{u}}{\bar{u}_e}\right) dy \quad (3)$$

$$H = \frac{\delta^*}{\theta} \quad (4)$$

Integrated values are determined using a trapezoidal numerical integration. Integrations that require knowledge of a parameter's value down to $y=0$ extrapolate the existing data to $y=0$ using two different methods, which are then averaged. A resultant C_F is calculated via the momentum defect between the upstream and downstream rakes via the Kármán Integral relation [10], i.e.

$$C_F = 2 * \frac{\theta_2 - \theta_1}{x_2 - x_1} \quad (5)$$

Additionally, the theoretical values of the thickness parameters θ and δ^* can be approximated using the following equations from White [11]:

$$\frac{\delta^*}{\delta} \approx \frac{1 + \Pi}{\kappa \lambda} \quad (6)$$

$$\frac{\theta}{\delta} \approx \frac{\delta^*}{\delta} - \frac{2 + 3.2\Pi + 1.5\Pi^2}{\kappa^2 \lambda^2} \quad (7)$$

$$\Pi = \frac{\kappa A}{2} \quad (8)$$

$$\lambda = (2/C_f)^{1/2} \quad (9)$$

Here, δ is equated to the measured experimental value. Per White and Coles [11, 12], $\kappa = 0.41$. The value of C_f is approximated by:

$$C_f \approx \frac{0.455}{\ln^2(0.06 Re_x)} \quad (10)$$

Note that the parameter A is an outer-law variable that varies with pressure gradient, and $A = (1.0, 2.5, 5.6, 13)$ corresponds to a strong favorable, flat plate, mild adverse, and strong adverse pressure gradient, respectively [11]. For this reason, a value of 2.5 is assigned to A for calculations in this paper. The value of Re_x is determined by the local Re measured experimentally at either rake. Once the theoretical values of δ^* and θ are approximated (based on the experimental Re_x and δ), they can be directly compared to the experimental values. Furthermore, the theoretical θ_2

and θ_1 determine the resultant theoretical C_F , based on the same experimental x_2 and x_1 . This is an agreeable means of comparison between the experimental and theoretical values of C_F .

An objective characterization of the longitudinal pressure gradient is provided by the Clauser parameter, β , defined [13, 14] as

$$\beta = \frac{\delta^*}{\tau_w} \frac{dp_e}{dx} \quad (11)$$

$$\tau_w = \frac{1}{2} \rho u_e^2 C_f \quad (12)$$

For use in comparison to theoretical velocity profiles, Spalding's Law of the Wall [15] is expressed as

$$y^+ = u^+ + e^{-\kappa B} [e^{\kappa u^+} - 1 - \kappa u^+ - \frac{(\kappa u^+)^2}{2} - \frac{(\kappa u^+)^3}{6}] \quad (13)$$

The constants $(\kappa, B) = (0.41, 5.0)$ per Coles and White [11, 12]. The friction velocity, u_τ , which appears in the calculation of u^+ and y^+ , is defined as

$$u_\tau = \left(\frac{\tau_w}{\rho} \right)^{1/2} \quad (14)$$

For the sake of completeness, τ_w , and hence u_τ , is calculated two different ways using either side of the Kármán Integral:

$$\frac{d\theta}{dx} + (2 + H) \frac{\theta}{u_e} \frac{du_e}{dx} = \frac{\tau_w}{\rho u_e^2} = \frac{C_f}{2} \quad (15)$$

In this paper, method *a* denotes calculation of τ_w (and u_τ) via the left side of Eq. 15, and method *b* the right. These two methods aid in calculating the dimensionless velocity profiles of the inner-law, as they depend on u_τ as well:

$$u^+ = \frac{\bar{u}}{u_\tau} \quad (16)$$

$$y^+ = \frac{y u_\tau}{\nu} \quad (17)$$

An extension of the log law, which is encapsulated within Spalding's Law of the Wall, is made for uniform rough surfaces with the following equation from White [11]:

$$u_{overlap}^+ = \frac{1}{\kappa} \ln(y^+) + B - \Delta B(k^+) \quad (18)$$

The first two terms form the typical log law, and the third term is a function of both the roughness type and the nondimensional flow quantity k^+ . For sand grains, e.g. the sandpaper used in this testing, White [11] defines the third term as

$$\Delta B \approx \frac{1}{\kappa} \ln(1 + 0.3k^+) \quad (19)$$

$$k^+ = \frac{k u_\tau}{\nu} \quad (20)$$

The variable k is the average roughness height of the sand grains, which is taken from tabulated values that match the particular grit sized used. In future tests, a more accurate k can be measured directly using specialized instruments.

The law-of-the-wall relations above for smooth surfaces, although plotted often in the literature, do not account for the wakelike component in the velocity profile of the outer layer. For this purpose, Coles' law of the wake [16] is employed

$$u^+ \approx \frac{1}{\kappa} \ln(y^+) + B + \frac{2\Pi}{\kappa} f\left(\frac{y}{\delta}\right) \quad (21)$$

$$f\left(\frac{y}{\delta}\right) \approx \sin^2\left(\frac{\pi y}{2\delta}\right) \quad (22)$$

The law of the wake is very useful to verify the wake component of the measured velocity profiles agrees with flat-plate turbulent boundary-layer theory and is not abnormal.

2. Assumptions

It is assumed that the static pressure is constant throughout the y -extent of the boundary layer at a given x -location and that the static temperature throughout the test section is constant and equal to that measured at the Pitot-static-temperature probe. Corrections are not made for the apparent height of rake Pitot probes. The small flow angularity and turbulence intensity in the test section are not taken into account in calculations. For the purpose of calculating parameters which are a function of the local skin friction coefficient, the value of C_f is approximated from Eq. (10). The value of k is taken from tables. The values of A , κ , and B are taken to be 2.5, 0.41, and 5.0, respectively.

III. Results

A. Diagnostics

The quality and repeatability of the flow and test fixture are established by a facility shakedown and comparison to flat-plate, turbulent boundary-layer theory for smooth and uniformly rough surfaces. The shakedown assesses longitudinal and lateral equivalent u_e variations along the splitter plate as a percentage of the free stream, β calculations to further examine pressure gradient severity, upstream rake unit Re against time, and upstream rake data independence of ψ . These indicators readily identify errant data and any required test-fixture adjustments.

1. Shakedown

The literature [e.g. 12-14] stresses the importance of two-dimensional test boundary layers. To ensure the test fixture is creating zero-pressure-gradient, two-dimensional, flat-plate flow, the u variation in x - and z -directions are evaluated. As seen in Fig. 6a, u_e is nearly constant along the length of the splitter plate after tuning the ceiling panels' and splitter plate pitch angles—flow deceleration near the splitter plate leading edge is not plotted to avoid confusion. Furthermore, Fig. 6b illustrates the near two-dimensionality of the flow just upstream of the disk.

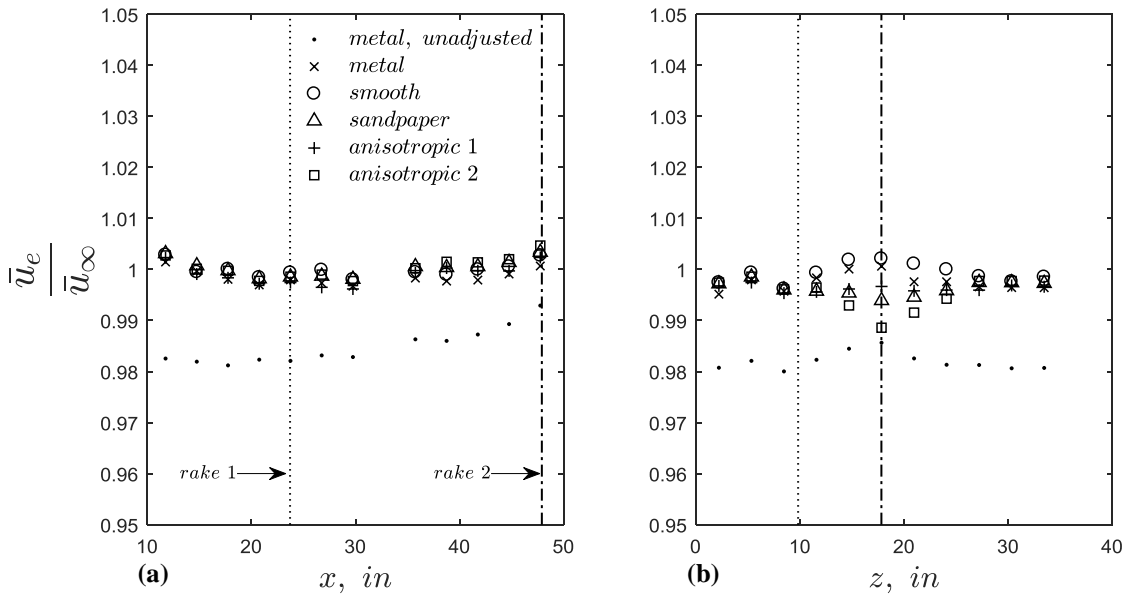


Fig. 6 Streamwise (a) and spanwise (b) edge velocity distributions

The results of the analysis on the longitudinal pressure gradient populate Table 2 and support the conclusion that this pressure gradient is insignificant. According to Clauser, $\beta = (-8, 0, 8)$ for a strong favorable pressure gradient, a zero-pressure-gradient, and a strong adverse pressure gradient, respectively. The results are all near $\beta = 0$, indicating a zero-pressure-gradient flow. It is important to note that the fact that β is (nearly) constant from rake 1 to rake 2 indicates the fixture creates a turbulent boundary-layer in equilibrium [13, 14].

The criticality of Re in assessment of C_F , evident by inspection of the many empirical and theoretical skin friction coefficient relations, necessitates a steady and repeatable Re setpoint. In consideration of the repeatability of the wind tunnel test conditions, Re_I values against time are plotted in Fig. 7 for all test runs (including both u_∞ -based and unit- Re -based wind tunnel control methods mentioned in Section II.C). The max difference in Re_I between any two points is approximately 2.3%. As expected, the unit- Re -based control method holds Re_I within a very tight variance ($C_v < 0.08\%$), while Re_I varies more over time ($C_v < 0.41\%$) in the u_∞ -based control method since u_∞ is not adjusted to compensate for changes in test section air temperature over long test durations. The presented data suggest that an acceptably small deviation in unit Re over a long test is achieved by either tunnel control method, although the clear choice for future testing is control by unit Re . A further testament to the repeatability of the test conditions and independence of rake 1 data on ψ is seen in Fig. 8, which illustrates the (lack of) variation in θ_1 measurements across

Table 2 β for each specimen

Specimen	β_1	β_2
Metal	0.00	-0.04
Smooth Film	-0.01	-0.05
Sandpaper	0.00	-0.07
Anisotropic 1	0.00	-0.08
Anisotropic 2	-0.01	-0.09

two weeks. A total of nearly 200 time-averaged measurements for the five different surface specimens and the two different wind tunnel control methods are presented.

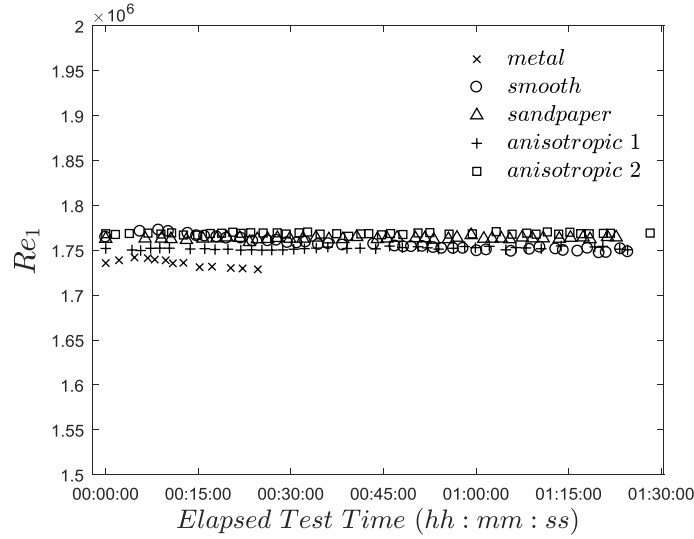


Fig. 7 Unit Re_1 over time for all test conditions

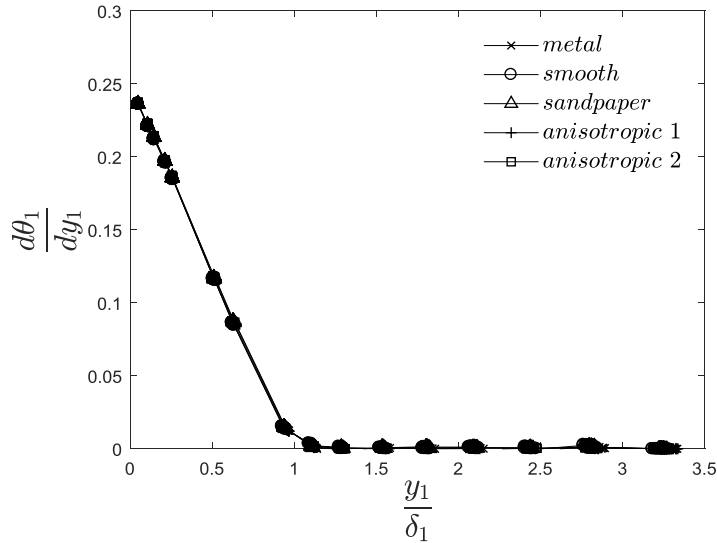


Fig. 8 Overlay of all $d\theta_1/dy_1$ vs y_1/δ_1 measurements for all specimens

2. Comparison to Theory

There are a variety of indicators from theory, some more involved than others, that guide the authors' conclusion of whether the flow over the splitter plate for the baseline and smooth film specimens can be deemed to develop as expected for smooth, flat-plate, turbulent boundary-layer theory. A simple (albeit not rigorous) check of the turbulent behavior of the flow is via the parameter H . Per Schlichting [17], $H \approx 2.59$ for laminar flows and $H \leq 1.4$ for turbulent flows. The data in Table 3 match the criterion for this turbulent flow characteristic, i.e. the test fixture and boundary layer trip strip are configured correctly to develop turbulent flow by the time the flow reaches the surface specimen, according to evaluation of H .

A more rigorous evaluation of agreement with smooth and rough, flat-plate, turbulent boundary-layer theory is achieved through comparison to theoretical velocity profiles, including Spalding's law of the wall, the log law adjusted

Table 3 H for smooth specimens

Surface	H_1	H_2
Metal	1.32	1.29
Smooth Film	1.32	1.29

for roughness, the velocity-defect law (or outer-layer defect law), and Coles' law of the wake. As is seen in Fig. 9, the experimental data for the smooth specimens agree quite well with Spalding's Law of the Wall with method a and b for calculating u_τ . Both methods also agree well with each other. Use of Eq. (18) permits the comparison of the experimental results of the sandpaper specimen to the log law adjusted for roughness based on the experimental k_s^+ . This result is also plotted in Fig. 9 and shows that the results of the sandpaper specimen agree well with the theoretical approximations for a uniform sand grain roughness of the same roughness height and test conditions.

Further comparison to theoretical profiles of the outer-law variable, or velocity-defect law, is illustrated in Fig 10.

The theoretical curves and experimental data agree very well. These particular profiles, as correlated by β and the theory of Mellor and Gibson [18], also offer reassurance that the pressure gradient along the length of the splitter plate is properly adjusted, as the data lay very near to the curve of $\beta = 0$. Additionally, the experimental velocity-defect law profiles are compared to various sources of the same data for smooth, flat-plate, turbulent-boundary-layer flow with varying pressure gradients. This compilation is overlaid in Fig. 11. Once again, the data from different sources compare very well, suggesting reasonable velocity profiles and zero-pressure-gradient flow for this test fixture and garnering confidence in subsequent test results. The final comparison employed is that between the experimental and theoretical law of the wake, which was proposed by Coles [16] to account for the wake-like deviations, or excess velocity, of the outer layer above the log layer. Such deviations are seen in Fig. 9. Coles' law of the wake, Eq. (21), offers a means to check if those deviations are nominal. Figure 12 illustrates the comparison between the law of the wake for theoretical profiles and the metal specimen experimental profile. The results are very encouraging as they show that the velocity profile of the metal specimen lay nearly on top of the theoretical profile for a flat plate specimen. The mean difference between the experimental law of the wake profile and the theoretical profile for $A = 2.5$ is approximately 2.1%, which reassures that the extent of the experimental velocity profiles, including the wake component, agree with theory. Recall from Section II.D.1 that $A = 2.5$ corresponds to a flat plate pressure gradient.

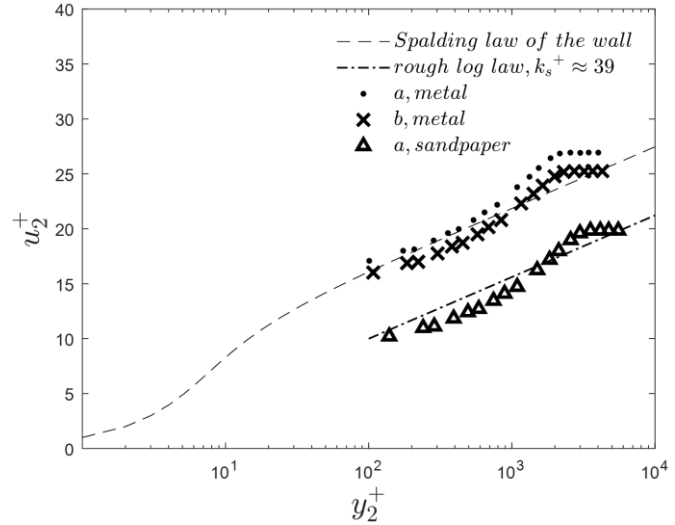


Fig. 9 Law-of-the-wall variables for the metal disk at rake 2

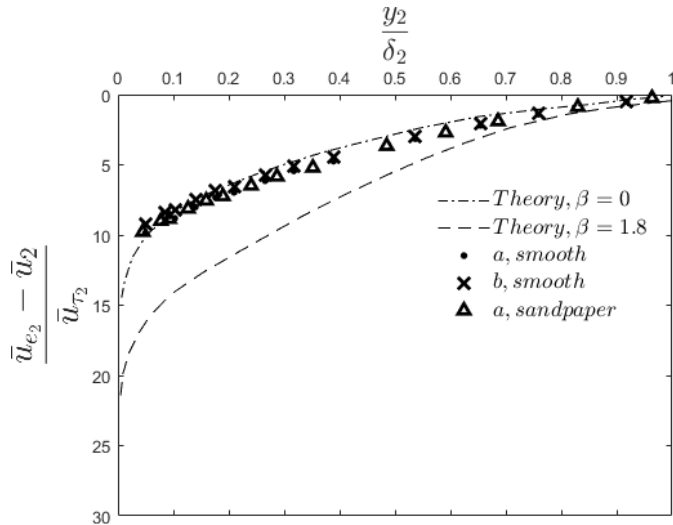


Fig. 10 Velocity-defect law of metal and sandpaper specimens compared to theoretical equilibrium-defect curves. Curves from work of Mellor and Gibson [18], digitized from White [11].

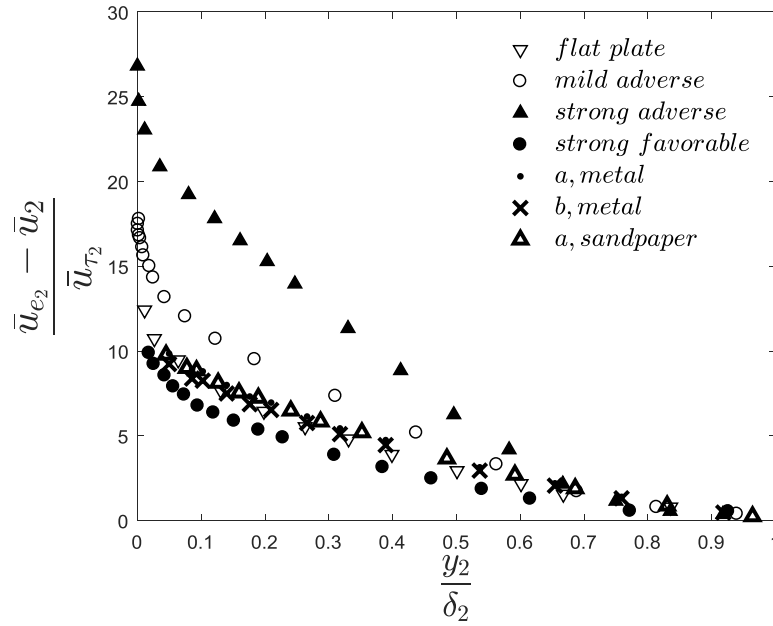


Fig. 11 Velocity-defect law for metal and sandpaper specimens compared to other experimental velocity-defect curves with varying pressure gradients. Other data compiled by and digitized from Refs. [11, 12].

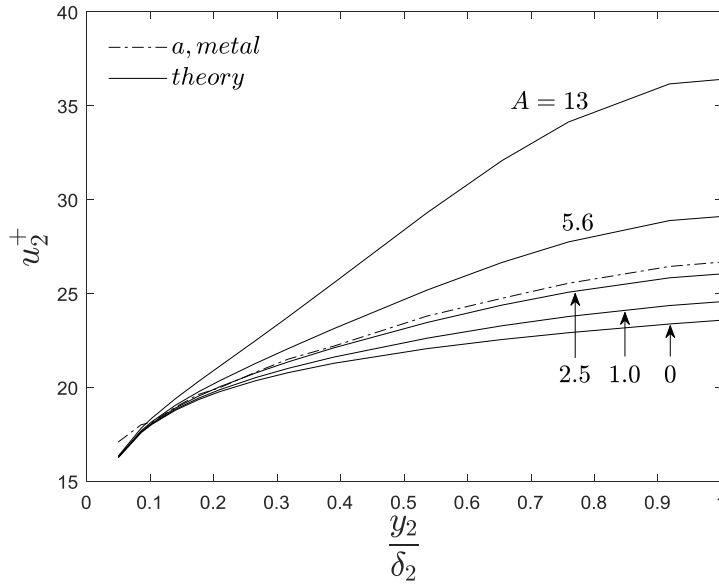


Fig. 12 Coles' law of the wake for the metal specimen and theoretical profiles with various values of A

B. Average Skin Friction Coefficient Measurements

The C_F of each surface specimen is calculated at each ψ to characterize the dependence of the former on the latter. One would expect that there would exist no such dependence for the metal, smooth film, and sandpaper specimens, as their patterns are uniform with respect to ψ . On the other hand, it is expected that the anisotropic specimens exhibit a unique dependence on their orientation to the flow. These expectations as well as comparisons between experimental and theoretical C_F are examined in this section.

1. Average Skin Friction Coefficient versus Flow Angle

Figure 12 illustrates the normalized comparison of all surface specimens' skin friction coefficients versus angle overlaid.

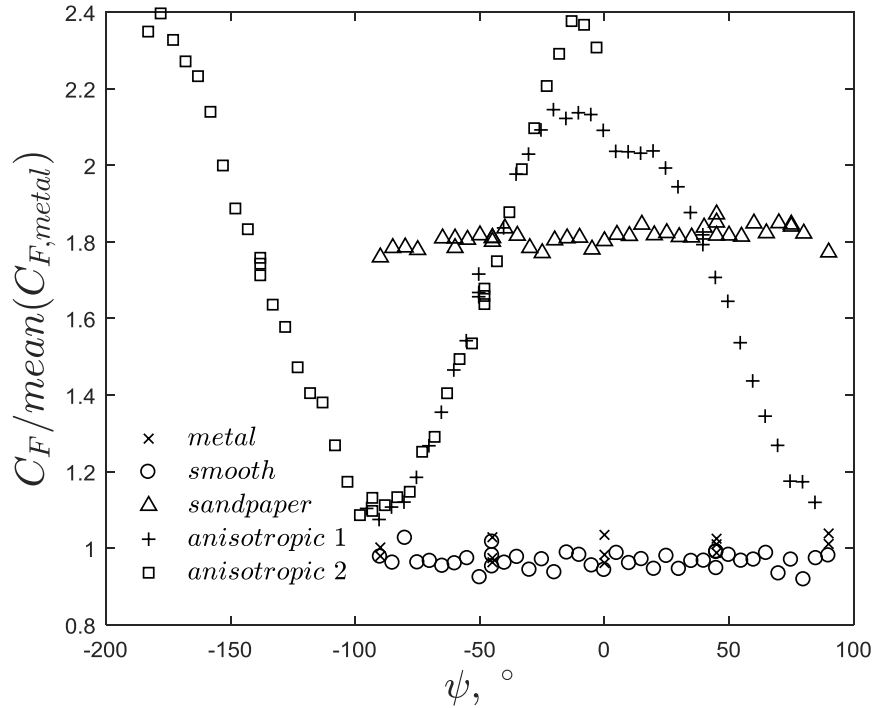


Fig. 13 Normalized C_F vs ψ for all tested specimens. C_F is normalized by the mean C_F of the metal specimen.

The C_F results align with intuition and classical expectations. The blank and smooth specimens produce the lowest C_F and their C_F are independent of flow angle (constant); the sandpaper specimen produces larger C_F than the former two specimens and is also independent of flow angle (constant). A significant finding is that the two anisotropic specimens produce the highest C_F and it is strongly dependent on flow angle. Statistical analysis shows that the dependency, or lack thereof, of C_F on angle for each surface specimen is significant, as discussed in Section III.C.1. Interestingly, the slopes of the two anisotropic specimens overlap very well for the range of $\psi \approx [-90^\circ, 25^\circ]$. Close to $\psi = 25^\circ$, $C_{F,\text{anisotropic 2}}$ exceeds $C_{F,\text{anisotropic 1}}$ until it reaches a factor of 2.4 larger than that of the metal specimen and a factor of approximately 1.33 larger than the sandpaper specimen. It is possible that there is a generic relation that could be modeled for this type of anisotropic specimen within an “overlapping” region of ψ . Furthermore, the large range in values of C_F confirms the value of estimating C_F as a function of ψ for anisotropic surface specimens.

It should be noted that anisotropic specimen 2 seems offset from other data—this is merely an artifact of the angle-designation convention and the orientation of specimen into the fixture upon installation. The asymmetry of anisotropic specimen 1 near $\psi = 0$ is believed to be due to seam effects, as this was the point in this specimen’s rotation that the seams (on the order of a quarter inch wide) were aligned with the flow and with rake 2. This result did garner interest in future studies to assess the impact of seams and gaps on C_F .

2. Theoretical Average Skin Friction Coefficient Values Compared to Experimental

The methods to calculate both the theoretical and experimental C_F are outlined in Section II.D.1 and employ Eqs. (1-10). The results of that procedure are tabulated in Table 4 for both the metal and smooth-film specimen.

Table 4. Percent difference between theoretical and experimental values with theoretical values as reference

Specimen	δ_1^*	δ_2^*	θ_1	θ_2	C_F
Metal	-4.73%	-3.87%	-8.44%	-7.42%	-5.80%
Smooth	-4.48%	-3.30%	-8.57%	-6.97%	-4.30%

The results are highly encouraging. All of the experimental boundary-layer parameter values agree with flat-plate turbulent boundary-layer theory to within 9%. The negative values for the percent differences mean that the theoretical values are less than the experimental values in all cases. The resultant experimental C_F agrees with theory to within 6%.

C. Statistical Assessment

In addition to the theoretical comparisons in Section III.A, more formal statistical analyses are performed to establish the confidence in the findings.

1. Dependence of the Average Skin Friction Coefficient on Flow Angle

A well-designed test fixture should demonstrate an independence of C_F on ψ for isotropic specimens and a dependence of C_F on ψ for anisotropic specimens. Figure 13 illustrates the statistical significance of the aforementioned independence for the smooth specimen.

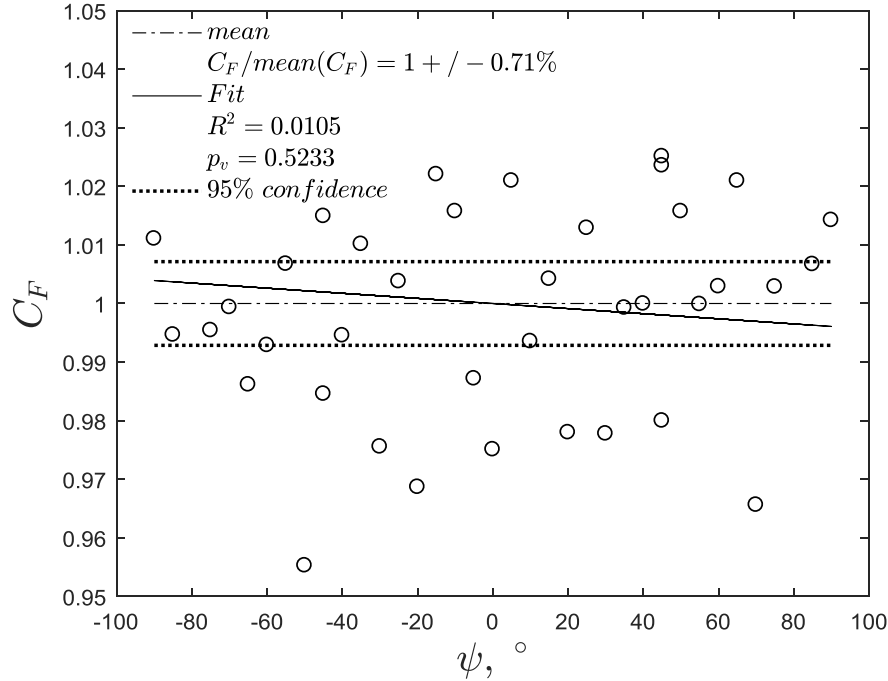


Fig. 14 C_F vs ψ for the smooth specimen with statistics

As seen in Fig. 14, the calculated C_F values for the smooth-film specimen produce agreeably-narrow 95-percent confidence bounds about the mean of all the C_F data ($C_{F,mean} \pm 0.71\%$). In essence, it is highly probable that the C_F value will lay within the plotted bounds. The data are fitted to a simple linear model, $C_F \sim 1 + \psi$, and the results suggest that a linear model is a poor fit of the data. This is supported by the very low R^2 value and the very high p_v , i.e. the fitted data variability or scatter in the data about the mean is not explained by the model and the fit is not statistically significant ($p_v > 0.05$). This confirms that, as expected, there is no linear dependence of C_F on ψ for this isotropic specimen. Furthermore, the scatter in the data does not suggest an obvious nonlinear dependence. A similar process is performed for each isotropic specimen and the all results show a statistically-significant independence of C_F on ψ and strong confidence in the mean. Furthermore, this analysis is extended to the anisotropic specimens with simple nonlinear models ($C_F \sim 1 + \psi + \psi^2$) and demonstrates, as expected, a statistically-significant nonlinear dependence of C_F on ψ .

2. Monte Carlo Simulation on Precision

A Monte Carlo simulation is a tool whereby one may propagate error to assess the effect on a resultant parameter. In this particular case, as-measured test-fixture measurement device precision is propagated throughout the C_F computation algorithm outlined in Section II.D.1 and represented as a probability density function (PDF) of C_F . Note that this only accounts for precision error and not potential bias in the measurements. Error is propagated on the following measurements: p_{rake} , p_{plate} , p_{pitot} , T , and the height of each rake probe, y_{rake} . The σ of p_{rake} , p_{plate} , p_{pitot} , and T are computed directly from test data, and y_{rake} is assigned a σ of 0.001 in. Note that the mean values of all the σ are obtained from all the probes of rake 1 across the N samples, and likewise for rake 2 and the splitter-plate static pressures. These values are used to calculate the P , defined by Ref. [19] as

$$P = \frac{P_0}{\sqrt{N}} \quad (23)$$

$$P_0 = K\sigma \quad (24)$$

The value of K equals 2 for a 95-percent confidence level. The P for each parameter is then used as a scaling function to a Gaussian distribution of $N = 100,000$. This creates a simulated dataset of N samples that are normally distributed with $\sigma = P$ and mean equal to the experimental mean and used to calculate N resultant C_F . Note that, among assuming a Gaussian distribution, this simulation also assumes the variables are independent and identically distributed. Also note this simulation is run on the smooth-film specimen since it has more data points than the metal specimen and each data point should ideally be at a quasi-constant pressure measurement due to its constant- u_∞ control, as discussed in Section II.C. The resultant PDF is seen in Fig. 15.

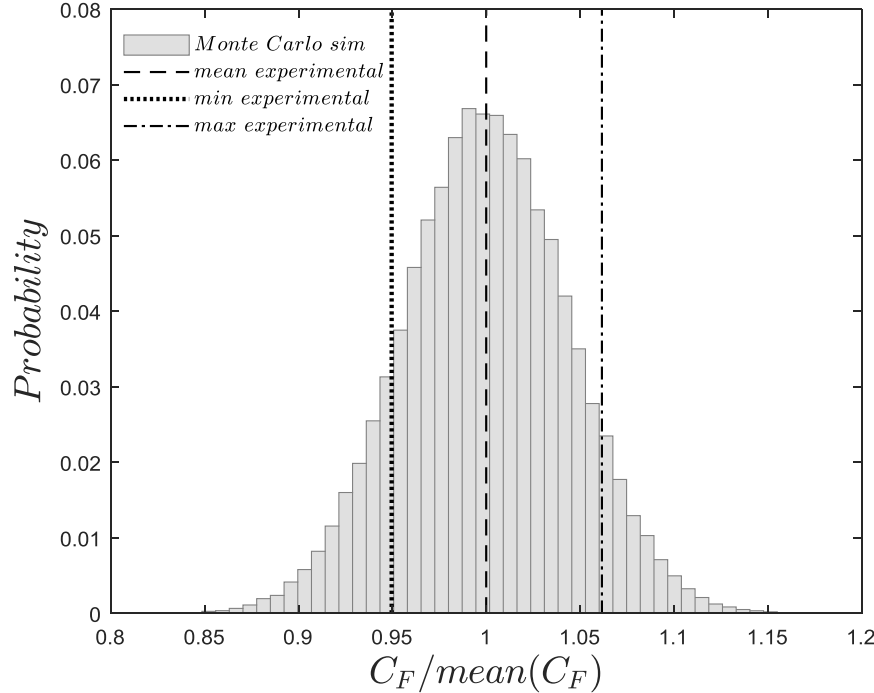


Fig. 15 Probability density function of smooth-film specimen C_F as simulated via Monte Carlo method for $N=100,000$ samples with means and standard deviations based on experimental means and precision limits

The main result is that the simulation predicts a band of C_F values that lay outside the minimum and maximum measured values for this specimen, i.e. the precision error propagation suggests that eventually this test fixture may measure values at the outer bands of the simulated measurements, albeit at a much lower probability. This tool is also useful to understand the sensitivities of the error propagation. It is found that the precision of the pressure measurements precisions is critical while the probe height and temperature precision are less critical in resultant C_F values. To narrow the simulated range of probable C_F values, higher-precision (i.e. higher-accuracy) pressure measurement devices are necessary.

IV. Conclusions

The need to readily characterize C_F for any given surface specimen and at any given ψ is apparent. To provide such a capability, BR&T and BT&E St. Louis have designed a unique test fixture and validated it with a rigorous testing campaign. This reliable test fixture is proved successful in its ability to effectively and efficiently estimate C_F over an arbitrary specimen surface and as a function of ψ with relatively little effort by the operator compared to alternative methods. Various diagnostics ensure the repeatability of the test conditions and the quality of the airflow in regards to its zero-longitudinal-pressure-gradient and two-dimensional turbulent boundary-layer development. Experimental data for the metal specimen, smooth film, and sandpaper specimens agree well with smooth and rough flat-plate, turbulent boundary-layer theory and confirm that the test fixture is well-designed. As expected, the metal and smooth film specimens produce nearly-identical C_F that is independent of ψ . The sandpaper produces higher C_F values than the metal and smooth film and it is also independent of ψ . The anisotropic specimens of similar feature height to the sandpaper produce larger C_F compared to sandpaper. As anticipated, the C_F of the anisotropic specimens does depend strongly on ψ . These findings are all statistically significant.

The testing process is streamlined and executed with Design of Experiments practices. Testing requires only two operators and a test duration of two hours for 180° ψ -sweeps at 5° increments including replicate conditions. Specimens are easily swapped with minimal downtime between specimen tests.

For future tests, the authors recommend 360° ψ -sweeps with more replicate conditions for a more complete dataset. Furthermore, test-fixture-dependent nonconformities like disk flatness and material seams must be minimized. That said, however, the present results suggest the feasibility to measure, in terms of C_F , the effect of specimen features, e.g. material gaps and seams. Future testing will measure plate static pressures and rake total pressures to within an accuracy of ± 0.00036 psi, or better.

Acknowledgments

The authors would like to thank the following individuals for their contribution to the success of this test capability: Jay Wiggins, Dave Benjamin, and Matt Michenfelder for their skill in wind tunnel test fixture design; Angelo Lucido for his expertise in wind tunnel instrumentation and test fixture installation; Dan Brzozowski for his diligence in wind-tunnel-control programming; and Tom VonHatten for his crucial consultation in boundary-layer trip strip design.

References

- [1] Fernholz, H. H., Janke, G., Schober, M., Wagner, P.M. and Warnack, D., "New developments and applications of skin-friction measuring techniques" *Journal of Measurement Science and Technology*, Vol. 7, No. 10, 12 Jun. 1996.
doi: 10.1088/0957-0233/7/10/010
- [2] Naughton, J. W., and Sheplak, M., "Modern developments in shear-stress measurement", *Progress in Aerospace Sciences*, Vol. 38, No. 6-7, Aug. 2002, pp. 515-570.
doi: 10.1016/S0376-0421(02)00031-3
- [3] Esteban, L. B., Dogan, E., Rodríguez-López, E. et al., "Skin-friction measurements in a turbulent boundary layer under the influence of free-stream turbulence" *Experiments in Fluids*, Vol. 58, No. 115, 2 Aug. 2017.
doi: 10.1007/s00348-017-2397-8
- [4] Lopper, D. J., and Rumsey, C. B., "Flight Measurements of Average Skin-Friction Coefficient on a Parabolic Body of Revolution (NACA RM-10) at Mach Numbers from 1.0 to 3.7," NACA RM L54G14, Aug. 1954.
- [5] Smith, D. W., and Walker, J. H., "Skin-Friction Measurements in Incompressible Flow," NASA TR-26, Feb. 1960.
- [6] Zuniga, F. A., Anderson, B. T., and Bertelrud, A. "Flight Test Results of Riblets at Supersonic Speeds, NASA TM 4387, 1992.
- [7] Braslow, A. L., and Knox, E. C., "Simplified Method for Determination of Critical Height of Distributed Roughness Particles for Boundary-Layer Transition at Mach Numbers from 0 to 5," NACA TN 4363, Sept. 1958.
- [8] Crawford, B. K., Duncan, G. T. Jr., West, D. E., Saric, W. S., "Laminar-Turbulent Boundary Layer Transition Imaging Using IR Thermography," *Optics and Photonics Journal*, Vol. 3, published online June 2013, pp. 233-239.
doi: 10.4236/opj.2013.33038
- [9] Raffel, M., and Merz, C. B., "Differential Infrared Thermography for Unsteady Boundary-Layer Transition Measurements", *AIAA Journal*, Vol. 52, No. 9, 2014, pp. 2090-2093.
- [10] Kármán, T. von, "Über laminare und turbulente Reibung," *Zeitschrift für angewandte Mathematik und Mechanik*, Vol. 1, No. 4, Aug. 1921 (English translation in NACA TM-1092).
- [11] White, F. M., *Viscous Fluid Flow*, 2nd ed., McGraw-Hill, New York, 1991.
- [12] Coles, D. E., and Hirst, E. A., "Computation of Turbulent Boundary Layers—1968 AFOSR-IFP Stanford Conference," *Proceedings 1968 Conference*, Vol. 2, Stanford University, Stanford, California, 1968.
- [13] Clauser, F. H., "Turbulent Boundary Layers in Adverse Pressure Gradients," *Journal of the Aeronautical Sciences*, Vol. 21, 1954, pp. 91-108.
- [14] Clauser, F. H., "The Turbulent Boundary Layer," *Advances in Applied Mechanics*, Vol. 4, Academic, New York, 1956, pp. 1-51.
- [15] Spalding, D. B., "A Single Formula for the Law of the Wall," *Journal of Applied Mechanics*, Vol. 28, 1961, pp. 455-457.
- [16] Coles, D., "The law of the wake in the turbulent boundary layer," *Journal of Fluid Mechanics*, Vol. 1, 191-226.
- [17] Schlichting, H., and Gersten, K., *Boundary Layer Theory*, 8th ed., Springer, Berlin, 2000.
- [18] Mellor, G. L., and Gibson, D. M., "Equilibrium Turbulent Boundary Layers," *Journal of Fluid Mechanics*, Vol. 24, 1966, pp. 225-253.
- [19] AIAA, "Assessment of Experimental Uncertainty With Application to Wind Tunnel Testing," AIAA S-071A-1999, Reston, VA., 1999.
doi: 10.2514/4.473647